SANDIA REPORT
SAND2007-6354
Unlimited Release
Printed October 2007

Terahertz Detectors for Long Wavelength Multi-Spectral Imaging

Eric A. Shaner, Albert D. Grine, Sungkwun K. Lyo, John L. Reno , and Michael C. Wanke

Prepared by
Sandia National Laboratories
Albuquerque, New Mexico 87185 and Livermore, California 94550

Sandia is a multiprogram laboratory operated by Sandia Corporation,
a Lockheed Martin Company, for the United States Department of Energy's
National Nuclear Security Administration under Contract DE-AC04-94AL85000.

Issued by Sandia National Laboratories, operated for the United States Department of Energy by Sandia Corporation.

Available to DOE and DOE contractors from
U.S. Department of Energy
Office of Scientific and Technical Information
P.O. Box 62
Oak Ridge, TN 37831

Telephone: (865) 576-8401
Facsimile: (865) 576-5728
E-Mail: reports@adonis.osti.gov
Online ordering: http://www.osti.gov/bridge

Available to the public from
U.S. Department of Commerce
National Technical Information Service
5285 Port Royal Rd.
Springfield, VA 22161

Telephone: (800) 553-6847
Facsimile: (703) 605-6900
E-Mail: orders@ntis.fedworld.gov
Online order: http://www.ntis.gov/help/ordermethods.asp?loc=7-4-0#online

SAND2007-6354
Unlimited Release
Printed October 2007

Terahertz Detectors for Long Wavelength Multi-Spectral Imaging

E. A. Shaner, A.D. Grine, S.K. Lyo, J.L. Reno, and M.C. Wanke

Sandia National Laboratories
P.O. Box 5800
Albuquerque, New Mexico 87185-MS1415

Abstract

The purpose of this work was to develop a wavelength tunable detector for Terahertz spectroscopy and imaging. Our approach was to utilize plasmons in the channel of a specially designed field-effect transistor called the grating-gate detector. Grating-gate detectors exhibit narrow-linewidth, broad spectral tunability through application of a gate bias, and no angular dependence in their photoresponse. As such, if suitable sensitivity can be attained, they are viable candidates for Terahertz mutli-spectral focal plane arrays. When this work began, grating-gate gate detectors, while having many promising characteristics, had a noise-equivalent power (NEP) of only 10^{-5} W/√Hz. Over the duration of this project, we have obtained a true NEP of 10^{-8} W/√Hz and a scaled NEP of 10^{-9}W/√Hz. The ultimate goal for these detectors is to reach a NEP in the $10^{-9 \rightarrow -10}$W/√Hz range; we have not yet seen a roadblock to continued improvement.

CONTENTS

NOMENCLATURE

THz	Terahertz, 10^{12}Hz
NEP	noise equivalent power
QW	Quantum Well
2DEG	Two-Dimensional Electron Gas
DOE	Department of Energy
SNL	Sandia National Laboratories

1. BACKGROUND

1.1. Motivation

There has been increased interest in the terahertz (THz, 10^{12}Hz) portion of the spectrum, particularly in the past 5-10 years, for a variety of security and sensing related applications. Despite this, devices commonly found in other regions of the spectrum, such as imaging arrays, have not been developed. Indeed, the THz world greatly desires a sensitive detector that can operate at normal incidence and at non-cryogenic temperatures. If the detector can have added spectroscopic capability, it could enable field applications which cannot be serviced through other techniques, such as Fourier Transform Infrared Spectroscopy. The goal of this work is to create such a detector having voltage controlled 'spectrometer on-a-chip' capability combined with normal incidence operation and a noise-equivalent-power in the $10^{-9 \rightarrow -10}$W/√Hz range.

1.2. Semiconductor Plasmons

Our detectors are based on two-dimensional plasmons in the channel of a field effect transistor (FET). Semiconductor plasmons are simply a charge oscillations having natural oscillation frequencies that depend on the carrier density. In a doped bulk (3-dimensional) semiconductor, it is well known that the plasma frequency is given by $\omega_p^2 = ne^2 / \varepsilon\varepsilon_0 m^*$. Where n is the carrier concentration, e is the charge of an electron, $\varepsilon\varepsilon_0$ is the background dielectric constant of the semiconductor, and m^* is the effective electron mass in the semiconductor. When the semiconductor system is reduced to two-dimensions, as in the channel of a field effect transistor, the screening dynamics are changed as charge electric field lines can fringe outside of the 2D layer. The end result is that the plasmon frequency now has a dispersion relation given by[1]:

$$\omega_p^2 = \frac{e^2 n(V_G) k}{2\varepsilon\varepsilon_0 m^*} \qquad (1)$$

where $n(V_G)$ is the 2D carrier density at a gate bias V_G, k is the plasmon wave vector, *and* ω_p , e, $\varepsilon\varepsilon_0$, and m^* are as previously defined. The presence of a gate metal above the transistor channel modifies the basic relation of equation 1 yielding[2]:

$$\omega_p^2 = \frac{e^2 n(V_G) k}{\varepsilon\varepsilon_0 (1 + \coth(kd)) m^*} \qquad (2)$$

Here d is the distance between the 2D transistor channel, and the gate metal. This typically results in a minor correction to the plasmon frequency, so in general throughout this document, equation 1 will be used for plasmon frequency calculations.

The most notable aspect of the plasmon dispersion relation is that frequency is proportional to the square root of both density and wave vector. This relation is used to identify plasmons as the resonant mechanism that is responsible for the photoresponse in grating-gate detectors. Typical electron densities of 10^{10} to 10^{12} cm^{-2} and device geometries of several microns in high-

mobility systems lead to plasmon modes in the ~ 1 THz range. This is where coupling to 2D plasmons can be seen as problematic. Typical THz wavelengths are on the order of several hundred microns, whereas the corresponding plasmon wavelengths are on the order of microns. The resulting severe wavevector ($2\pi/\lambda$) mismatch means that radiation does not naturally couple to the plasmons. However, the use of a grating, with a period matched to the plasmon wavelength, spatially modulates the incident radiation and permits coupling of THz radiation to plasmon modes[3]. While this technique was applied almost three decades ago in order to observe 2D plasmons in semicondcutors[3], to date, we have yet to see truly useful photodetectors based on these principles.

1.3: Work prior to this LDRD

As mentioned in section 1.2, many years prior to our work, 2D semiconductor plasmons had been observed[3]. In 2002, a double quantum well grating-gate detector had been demonstrated, in a collaboration between Sandia and UCSB[4]. This detector was shown to have a voltage tunable photoresponse[4] as demonstrated in fig. 1.

While the tunable photoresponse was a nice result, the noise equivalent power (NEP) was only 10^{-5}W/√Hz, 5 orders of magnitude worse than where it is desired to be. Beyond this, the dynamics underlying the photoresponse were not understood. Corresponding measurements done at the time also indicated that the double quantum well (as opposed to a single quantum well which is closer to a standard field effect transistor) was absolutely necessary in order to observe a photoresponse.

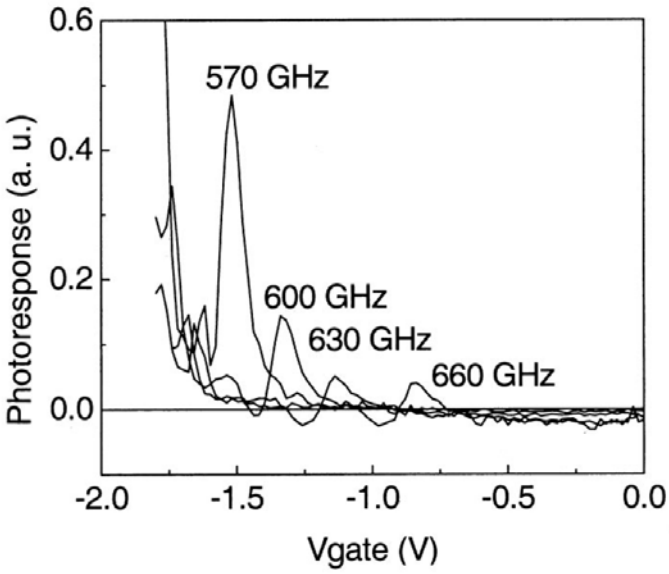

Fig. 1: Photoresponse of a double quantum well grating gate detector to different frequencies radiation. As the gate bias is changed, the frequency of the plasmon resonance in the device changes. When there is a match between the plasmon frequency and the radiation frequency, a peak is seen in the photoresponse.

2. ACCOMPLISHMENTS

This section highlights the major accomplishments of our work. While many device geometries and materials were tried over the duration of this project, this section will not cover intermediate steps. More detailed fabrication information can be found in Appendix B.

2.1: Single Quantum Well Detectors

Double quantum well systems can be somewhat complicated. Transport properties of such systems depend not only on the physical properties of each well, but also on their spacing. As such, at the outset of this work, most milestones in year 1 dealt with understanding how double quantum well parameters affected detector response and performance. These were almost immediately redirected as we found out early on in the work that single quantum well detectors functioned in the same way as the double quantum well detectors discussed in section 1.3. This was an important finding mainly because plasmons are a relatively understudied topic and the physics of a single quantum well is much easier to understand compared to double well systems. Beyond this, it is far simpler to fabricate other structures, such as on-chip amplifiers, from single quantum well material.

Figure 2 shows the typical geometry of a grating gate detector. This device is essentially a field-effect transistor (FET). It is comprised of source (S) and drain (D) ohmic contacts and has a gate (G) for controlling carrier density. The primary difference between the grating-gate detector and a typical FET is that the gate is huge (2mm x 2mm as shown) and it is also modulated (zoomed view). The reason for the large gate area is simply to match typical THz spot sizes (1mm - 2mm). The purpose of the gate modulation is to both modulate the carrier density in the channel and also to modulate incident radiation, as discussed in section 1.2, to allow coupling of radiation to plasmon modes.

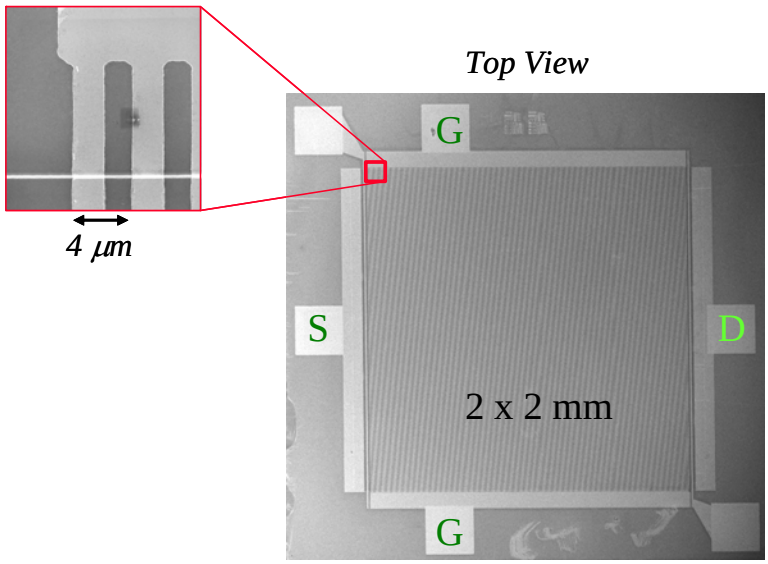

Fig. 2:Geometry of the grating-gate detector. Zoomed view shows the fine detail of the 2mm x 2mm grating having a 4μm period.

In this work, the grating-gated FETs are fabricated from a single modulation-doped GaAs-AlGaAs quantum well (QW), 40 nm wide, formed 200 nm below the wafer surface. The QW had approximate two-dimensional electron gas (2DEG) electron density of 2.5 x 10^{11} cm^{-2} and mobility $\mu \approx 5 \times 10^6$ $cm^2/V \cdot s$. The device was fabricated on an isolation mesa etched completely though the 2DEG. Standard annealed Ohmic contacts form the source and drain. The grating

gate is comprised of 20 nm Ti and 50 nm Au and has a 4 μm, 50% duty cycle period over a 2 mm x 2 mm area. When this gate is biased with respect to the underlying QW, it creates a non-uniform spatially modulated carrier density. Under these conditions, the coupling to resonant plasmon modes produces an electrical photoresponse that displays a rich spectrum of behavior depending on incident power, plasmon mode index, and source-drain bias current.

The dispersion relation for 2D plasmon resonances in a heterostructure FET is given by[1]

$$f_0^2 = \frac{1}{4\pi^2}\frac{e^2 n(V_G) k_j}{2\varepsilon\varepsilon_0 m^*} \qquad (3)$$

where f_0 is the resonance frequency, e is the electron charge, $n(V_G)$ is the 2DEG density at a gate bias V_G, $k_j = jk_1$ is the j^{th} harmonic mode of the plasmon wave vector (j = 1, 2, 3,...), $\varepsilon\varepsilon_0$ is the dielectric constant of the semiconductor, and m^* is the effective electron mass. For the THz detectors discussed here, the lowest wavevector $k_1 = 2\pi/4$ μm is fixed by the 4 μm period of the grating gate, (2 μm metal + 2 μm gap) and corresponds to half a plasmon wavelength fitting underneath the gate metal line.

From Eq. 3, for a single incident THz frequency resonance may occur at different densities for different spatial harmonics k_j. Thus there may be multiple plasmon resonances available in the device at different carrier densities or gate biases. Furthermore, at a particular plasmon mode j the square of the resonant frequency should be linearly dependent on carrier density alone.

Measurements were made using two distinct THz sources that overlapped in frequency but permitted a wide range of power: 1.) a continuous wave (CW) molecular gas far-infrared laser, and 2.) a widely tunable pulsed free-electron laser (FEL). The electrical response measurement was essentially identical in both cases. A bias current (I_{SD}) was applied between the source and drain with the drain grounded, while a gate voltage bias (V_G) was applied with respect to the drain. Additional source and drain leads were used for signal detection in a quasi-four point arrangement. In the CW case, the signal leads were fed into a lock-in amplifier referenced to a 390 Hz chopping frequency. For the FEL measurements, the signal leads were buffered by a differential amplifier before being read by a high-speed digitizing oscilloscope.

Fig. 3 shows the T = 20 K device CW photoresponse vs. V_G at three different I_{SD} using 763 GHz illumination. Clear peaks are observed around V_G = –0.32V and –0.53V, corresponding to two plasmon modes at this one frequency. The DC pinchoff voltage, V_P, is near –0.75V. As V_G approaches V_P, the response magnitude is seen to increase as previously observed in DQW grating gate detectors. One interesting feature of this data is the large resonant signal when I_{SD} = 0, indicating a mostly photovoltaic (PV) response. For I_{SD} = +200 μA the PV signal peaks shift slightly to the right. The peak

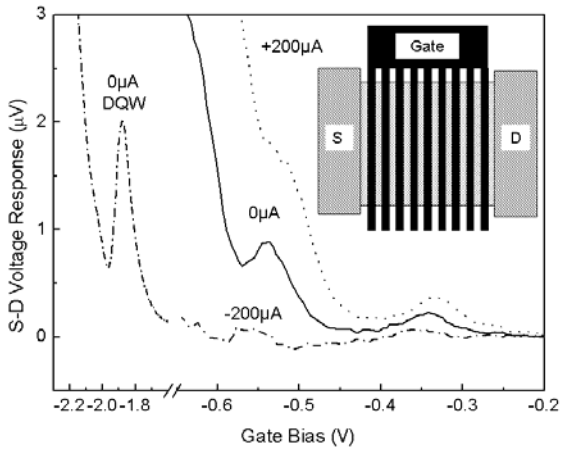

Fig. 3. Photoresponse of single and double quantum well detectors. The single well data spans from -0.2 to -0.65V and is shown at three different source-drain currents. The double well detector is shown from -1.6 to -2.2V at I_{SD} = 0. Measurements were taken using a CW source at 763 GHz. In this setup, with a few mW incident power, there is a clear photovoltaic signal present at I_{SD} = 0 for both types of detectors.

shifting is consistent with a gradient in effective gate bias due to the source-drain voltage drop. For I_{SD} = –200 μA, the resonant response remains positive-going, again indicating a mostly PV response. In previous DQW detector work the primary response was observed to be mostly photoconductive (PC)[4]. In contrast, under the measurement conditions used here, the photoresponse of a DQW device shown in Fig.3 at I_{SD} = 0 is photovoltaic. This PV behavior of both single and double well detectors under the same experimental conditions has been consistently observed. Overall, this leads us to believe that both single and double well responses are based on the same physical mechanisms.

The observation of the large, broadband PV response close to V_P also prompts a reevaluation of the physical processes responsible. It was previously proposed that this pinchoff behavior in a DQW detector arises from a bolometric mechanism, a conclusion based on the broadband character of the response and on the very similar behavior of the responsivity and the temperature slope of the source-drain resistance, dR_{SD}/dT, both as a function of V_G near 4 K. However, a strictly bolometric response cannot give rise to a PV signal. Examining Eq. 1, the number of modes per change in electron density increases rapidly as the gated carrier density approaches zero at V_P. This compression of mode spacing and the consequent overlap of higher order peaks as $V_G \rightarrow V_P$ allows for the excitation of many closely spaced plasmon modes for any frequency and may explain the broadband response and increasing responsivity near pinch-off. Since each low order mode has demonstrated a PV response in the single-well detectors, a superposition of multiple simultaneously excited higher order modes may also explain the pinch-off PV response observed. The previous correlation of the response tracking dR_{SD}/dT may be coincidental, but it is possible the pinchoff response could well be a combination of both bolometric and higher mode excitation effects, with relative contributions depending on temperature, bias conditions, and illumination power.

The frequency and power dependencies were investigated with the FEL, which provided 2 μs pulses with peak power of approximately 1 kW that were strongly attenuated before being focused directly onto the sample. A software boxcar technique sampled the peak signal height of the photoresponse. This peak is the signal amplitude in Fig. 4 which shows the photoresponse (for I_{SD} = 100 μA) at two different power attenuation levels: *A* (–36 dB attenuation) and *B* (–16 dB attenuation). Three frequencies, 420, 450, and 600 GHz, were characterized at power *A*. In Fig. 4 arrows mark plasmon modes having the largest response. At power *B* (420 and 450 GHz shown), the peaks found at power *A* between –0.5V to –0.6V are smeared out. In both cases, as frequency is increased, the resonant peaks shift towards V_G = 0 (*i.e.* higher density) in accordance with Eq. 3. Over the range of attenuations used (10 dB to 55 dB) varying amounts of PV and PC contributions to the photoresponse were observed.

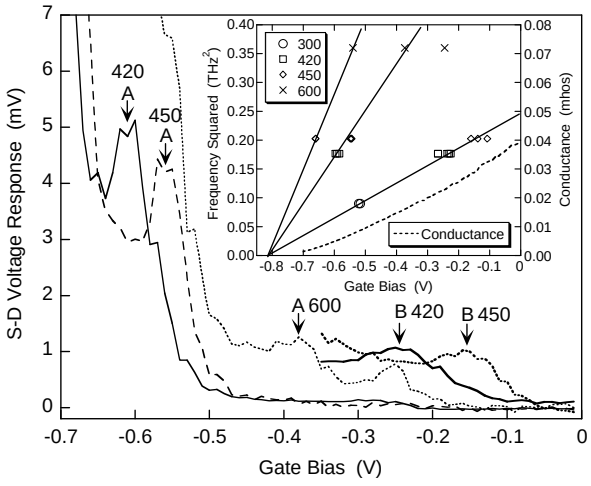

Fig. 4: Photoresponse at different wavelengths using I_{SD}=100 μA. The inset shows peak position vs, V_G from a larger set of FEL data. Lines drawn through the peak points extrapolate back to near the conductance pinchoff voltage.

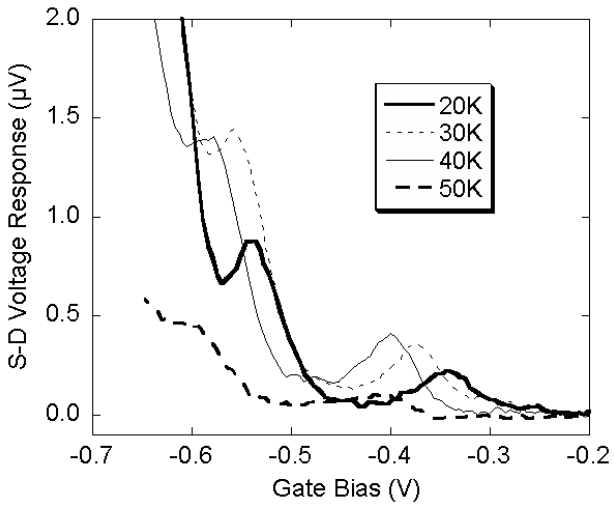

Fig. 5: Temperature dependence of photovoltaic response. As T increases from 20 K, the resonant peaks shift closer to pinchoff. The responsivity of the peak between –0.35V and –0.45V peaks between 30K and 40K and then rapidly falls off as T was increased further.

Fig. 4 inset plots observed resonant peak V_G vs. square of illumination frequency at 300, 420, 450, and 600 GHz over all the power ranges measured using I_{SD} = +100 μA. With the exception of one 600 GHz peak near –0.25V gate bias, the data fall onto three separate lines which all intersect at zero frequency at V_G = –0.80 V, nearly the same as the DC conductance pinchoff voltage V_P = –0.75 V. These linear dependencies and extrapolation to zero frequency at pinchoff follow very well the plasmon dispersion form of Eq. 1 if we take $n \propto (V_G - V_P)$. Empirically, the slopes of the three lines in Fig. 4 have ratio 1 : 2.8 : 4.6, which is close to the 1 : 3 : 5 ratio expected from Eq. 1 for the j = 1, 3, and 5 modes. Extrapolating the lowest mode to zero gate bias yields an ungated plasma frequency of 490 GHz. This is only a 15% discrepancy with the 425 GHz plasma frequency of the ungated j = 1 mode calculated from Eq. 3, providing an independent check on our assignment of mode number.

Similar to the DQW plasmon detectors originally investigated, these single-well detectors show a responsivity maximum at elevated temperatures. Fig. 5 shows the response of a single-well detector at 763 GHz in the CW setup from T = 20 to 50 K. The data were measured with I_{SD} = 0 (*i.e.* PV response), but other currents showed similar temperature behavior. As T is increased from 20 K, the resonance near –0.35 V shifts towards pinchoff. The responsivity of this mode peaks between 30 and 40 K before dying off at 50 K. It is difficult to describe the behavior of the mode near –0.55V as the temperature change shifts its position into the pinch off regime. The mechanism behind this unusual temperature dependence is not presently understood.

While overall the discovery that single quantum well material works in the same manner as double quantum well material for grating-gate detectors, they still suffer from the same problems. Namely, the noise equivalent power is still 10^{-5}W/√Hz. Because of this, we began attempts at new styles of detectors, based on the mechanisms in grating-gate detectors, in order to achieve better performance. As such, this work marked the end of study in terms of grating-gate detectors having a single gate.

2.2: The Split Grating-Gate detector

2.2.1: The Split Grating-Gate detector

As mentioned at the end of section 2.1, the performance of standard single well grating-gate detectors was sub-par. However, important knowledge was garnered from that work. The fact that single well detectors worked being one key point. The other important is that the response of the detector increased dramatically as the FET channel was gated into pinchoff. This improved response however, comes at the cost of losing all tunable aspects of the detector photoresponse. This situation inspired the creation of the split grating-gate detector.

A typical split grating-gate detector is shown in Fig. 6. Again, it consists of ohmic source (S) and drain (D) contacts, however, now the grating is split into three sections labeled V_{GS}, V_{FG}, and V_{GD}. The purpose of this device is to use a single gate line (V_{FG}) which bissects the device, and bias it to pinchoff to get the enhanced resposivity found in the pinchoff regime of standard grating gate detectors, while using the large gates V_{GS} and V_{GD} to provide resonant tuning While the initial plan was simple, it turned out the introduction of the single finger gate, V_{FG}, introduced some surprising behavior.

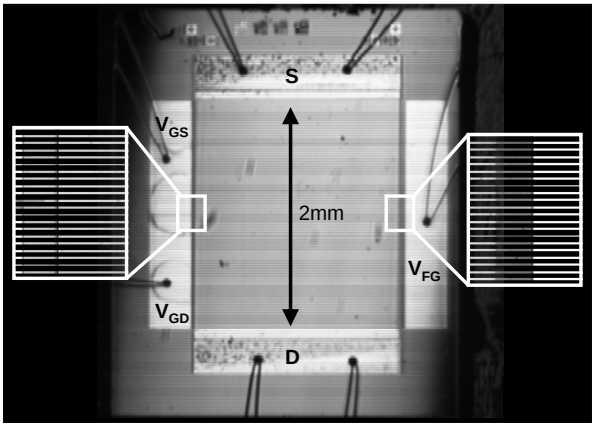

Fig. 6: Split gate detector with 2mm x 2mm grating gate area. The period of grating is 4μm, grating lines are 2μm wide. The zoomed regions show the detail of the split gate structure.

The grating parameters and device fabrication were the same as implemented in the device of section 2.1 (d = 4 μm, 2 μm metal and 2 μm gap). Devices were fabricated from single-QW GaAs-AlGaAs heterostructures, grown by molecular beam epitaxy and consisting of one modulation-doped GaAs well, 40 nm wide, formed 200 nm below the wafer surface. The QW had n = 2.5 x 10^{11} cm^{-2} and mobility $\mu \approx$ 5 x 10^6 $cm^2/V{\cdot}s$ at 4 K. Devices were isolated on mesas etched completely through the QW. Standard annealed ohmic contacts form source and drain. The gate metallization is comprised of 20 nm Ti and 50 nm Au.

Fig. 7 shows the source-drain current-voltage (I_{SD}-V_{SD}) characteristics of a QW FET at various finger gate biases V_{FG}. Here the source and drain gates were shorted to the source and drain contacts respectively. When $V_{FG} \geq -0.8$ V, I_{SD}-V_{SD} is ohmic (10 to 100 Ω). Increasing negative bias on the finger gate pinches off a 2 μm stripe down the channel center, and I_{SD}-V_{SD} takes on diode-like nonlinear characteristics strongly dependent on V_{FG}. This is consistent with tunneling and thermionic emission across a barrier beneath the finger gate whose barrier height depends on V_{FG}. The asymmetry arises from the fact that V_{FG} is referenced with respect to the drain. Points A, B, C, and D in Fig. 7 mark different bias points for THz response measurements.

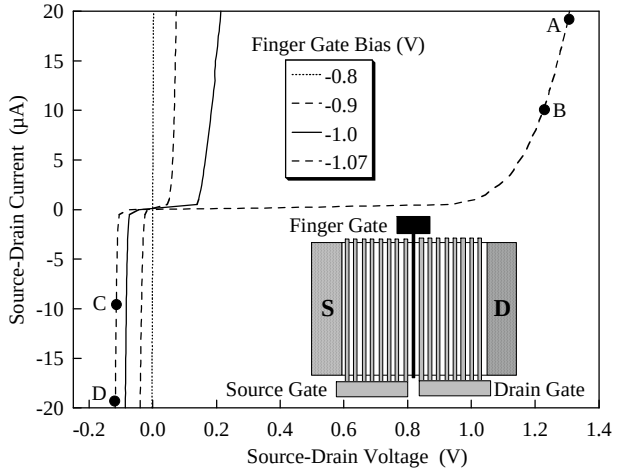

Fig.7: Source-drain current-voltage characteristics (in the dark) of the QW FET in split-gate operation at various values of the finger gate bias with respect to the drain. A, B, C, and D indicate operating points for the FIR response measurements shown in Fig. 2(a). Inset: schematic plan view of the QW FET split-gate configuration (not to scale).

THz response was measured with a CO_2-pumped molecular gas laser using formic acid vapor. THz light was focused via metal optics and split by a Mylar beamsplitter to both the QW FET and a pyroelectric meter that monitored relative changes in THZ output power. The THZ light was chopped at 385 Hz and detected

signals measured using lock-in techniques. Wavelength was measured with a Fabry-Perot interferometer. The QW FET temperature was 20 K. We observed plasmon resonances up to 70 K with decreasing quality factor and a small shift in resonance positions related to the temperature dependence of *n*. Near 20 K, the plasmon response is stable enough so that precise temperature control is unimportant.

Fig. 8(a) inset shows the QW FET response to 432 μm. Approximately 1.5 mW of THZ power was incident at the position of the QW FET. The power absorbed was not determined, but the response amplitude varied linearly with incident power near this power level. Here, all gates were tied to one voltage source. This configuration is identical to the single-gate design of section 2.1 and produces the same results: a pair of resonant plasmon peaks near V_G = –0.35 V and –0.5 V, corresponding to two spatial harmonics of the resonance described by (1). There is also a steep rise in response at more negative V_G that is not sensitive to THZ frequency. The two plasmon peaks have signal amplitudes of 0.8 and 3.2 μV.

Figure 8(a) shows the same QW FET under identical experimental conditions, except now the device is operated in split-gate mode with the finger gate biased separately from the source- and drain-side grating gates. The source gate bias V_{SG} is referred to the source contact bias V_S, and the drain gate bias V_{DG} is referred to the drain bias V_D. The bias circuitry maintained ($V_{SG} - V_S$) = ($V_{DG} - V_D$), which is the gate bias given in the plot. This nominally keeps the electron density and hence plasmon resonance identical in both source and drain regions. V_S and V_{FG} are both referenced to the drain, which is defined as the device common. V_{FG} = –1.07 V for all traces, with points A, B, C, and D corresponding to the labeled source-drain dc bias operating points of Fig. 7.

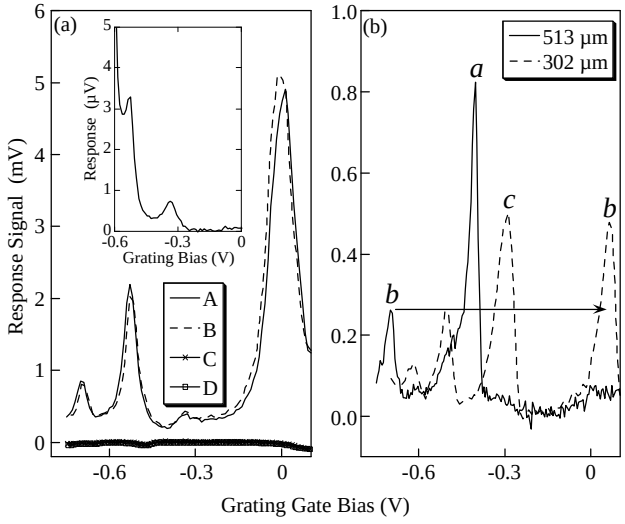

Fig. 8. (a) FIR response to 432 μm as a function of grating gate bias in the two operating modes. Inset shows response in single-gate mode. Main figure shows operation in split-gate mode with finger bias = –1.07 V. The curves A. B. C. and D correspond to the source-drain dc operating biases shown in Fig. 1. (b) FIR response of the same device in split-gate mode to 513 and 302 μm. Peak labels *a, b, c* indicate the harmonic mode to which each peak corresponds as mapped out in Fig. 3 inset. The arrow indicates how the *b* mode peak moves as wavelength is decreased.

Resonances near V_G = 0 V, –0.5 V and –0.7 V in curves A and B are nearly 10^3 times larger than the resonances shown in the inset at the same incident THZ power, along with a possible smaller resonance at –0.35 V. Interestingly, bias points C and D in Fig. 7, where the *I-V* characteristics are more strongly nonlinear than points A and B, produced much weaker resonant response. This is not expected for diode-like detectors. This suggests a fundamental difference between conventional drift electron diode response, which must follow the *I-V* of Fig. 7, and resonant plasmon response observed, which need not follow the dc *I-V*.

Comparing Fig 8(a) and its inset, a few differences are apparent. First, in split-gate operation, a new spatial harmonic of the resonance appears near V_G = 0 V.

Also, the other peaks shift slightly from their positions in single-gate operation. Finally, split-gate mode does not enhance equally all peak responses compared to single-gate operation.

Fig. 8(b) shows that the QW FET in split-gate mode retains gate-bias tunability. Three other wavelengths: 302, 395, and 513 μm, were shone on the same device, but for clarity only the 302 and 513 μm data are plotted. Illumination power varied with wavelength, but the resonant response amplitude was always 10^2 to 10^3 larger for split-gate operation compared to the same experimental parameters in single-gate mode. The labels *a*, *b*, and *c* designate which spatial harmonic modes the peaks at the different wavelengths belong to, as mapped out in the inset of Fig. 9 for all four wavelengths used. As THZ wavelength decreases from 513 to 302 μm, all peaks corresponding to the same mode move continuously towards more positive gate bias (*i.e.*, to larger *n*), as expected from (1). The peak labeled *a* moves to the right until it goes off scale, the peak labeled *b* moves as indicated by the arrow, and higher modes like peak *c* enter from the left.

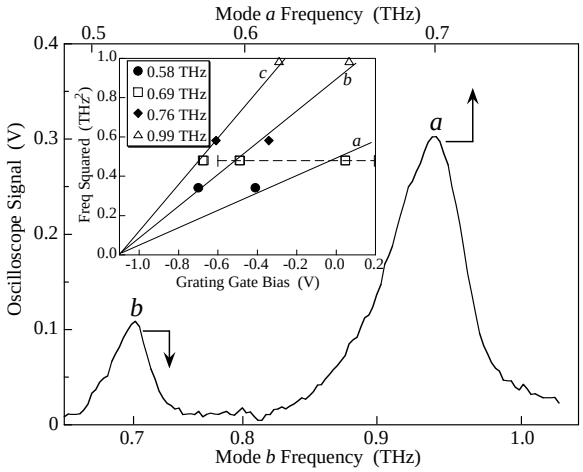

Fig. 9. Inset: Plasmon mode map showing how resonances fit to the dispersion relation of Eq.3. The line fits *a*, *b*, and *c* group the data into three modes. The dashed line indicates the range of the gate bias sweep used to generate the main figure, which covers two 432 μm modes. Frequency scales in the main figure are obtained from gate bias via the slopes of the *a* and *b* lines. Main: Spectrum of two plasmon modes excited by 432 μm light. The grating gate was swept from –0.6 to +0.2 V in 12.5 ms. The peak labeled *a* corresponds to the *a* line of the inset and uses the upper frequency scale, while the peak labeled *b* corresponds to the *b* line of the inset and uses the lower frequency scale.

In split-gate operation of the QW FET, the plasmon response is large enough and the parasitic reactance small enough that the gates can be swept to record a spectrum with video rate compatible acquisition time. Figure 9 shows the QW FET response to 432 μm illumination as recorded on an oscilloscope. Here V_{FG} = –1.07 V and the grating gates were ramped from –0.6 V to +0.2 V in 12.5 ms. The signal was put through a 10x gain pre-amp and into the scope. The figure displays the *difference* between the illuminated QW FET source-drain conductance, as the gate voltage is swept, and a "dark" trace of the same. The signal-to-noise ratio is > 10 dB, limited here by the recording electronics.

Two spatial harmonic modes, marked *a* and *b*, of the 432 μm resonances are clearly seen and correspond to the modes labeled *a* and *b* in Fig. 8(b). The families of spatial modes are displayed in the inset of Fig. 9, which plots the square of illumination frequency vs. the gate bias positions at which resonances were observed. From the plasmon dispersion in Eq. 3, the data are expected to fall on a family of lines, each line corresponding to a different spatial harmonic, intersecting zero frequency at a common threshold. Three such spatial harmonic lines labeled *a*, *b*, and *c* are shown all intersecting zero frequency near –1.1 V. This data can be used to convert gate bias to frequency scale, each mode having a separate frequency scale. Modes *a* and *b* were used to

generate the frequency scale for the corresponding resonance modes marked *a* and *b* in the main figure.

While the split grating-gate detector of this work demonstrated a responsivity that was improved by a factor of 1000, the noise equivalent power improved only by a factor of 100 to 10^{-7}W/√Hz. This is due to the fact that the pinched off single finger gate produces more electrical noise than the standard grating-gate detector of section 2.1. The end result is that, even though the split grating-gate detector offered significantly improved performance over its predecessors, more work was needed.

2.2.2 Split Grating-gate detector, small active region

Figure 10 shows the photoresponse of the split-gate detector discussed in the previous section (picture in Fig. 6) to 993 GHz radiation. The inset of Fig. 10 shows the I-V characteristics of this detector at T=20K when V_{FG} = -1.04V, about 300mV past the pinchoff voltage, with V_{GS} tied to the source contact and V_{GD} tied to the drain contact (zero effective gate bias on the source and drain side channels) in a common drain configuration. Under these conditions, one can see the detector exhibits diode like characteristics due to the barrier formed between source and drain. While the photoresponse mechanisms related to this barrier are still under investigation, it is thought that the quadrant of positive current/voltage (from source to drain) yields a bolometric photoresponse and the negative current/voltage quadrant may produce a rectified response.

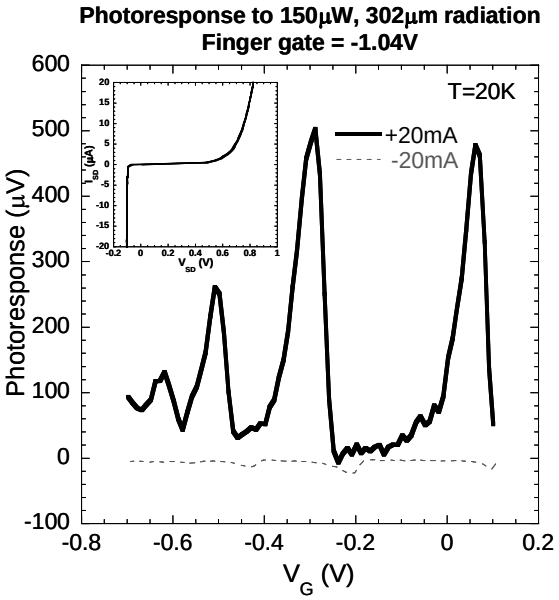

Fig. 10: 1THz photoresponse as a function of gate voltage. Inset shows the I-V characteristics of the split grating-gate detector when the tuning gate bias is 0V and the finger gate bias is -1.04V. The main plot shows the resonant photoresponse to 1THz as the tuning gate bias, V_G, is swept.

As in section 2.2.1, for measurements, the sample is illuminated, using f/2 focusing optics, by a CO_2 pumped far-infrared laser operating on the lines of formic acid. The response to 302μm radiation (~1THz) is shown in Fig. 10 with V_{FG} = -1.04V. An adding circuit is used to feedback the source drain voltage, V_{SD}, to the large gate on the source side of the single finger. This is done to create the condition that $V_{GS}=V_{GD}=V_G$, the tuning gate voltage. As V_G is swept, the portions of the channel under the grating gate lines are depleted, reducing the carrier density. When the conditions of Eq.3 are met, we get resonant plasmon peaks in the photoresponse.

With f/2 optics, and a 1THz laser line, a diffraction limited spot size of about 1.5mm is expected. Since this is smaller than the detector area (2mm x 2mm), such a configuration can be used to roughly map out the active area of the detector by moving the detector in the focal plane and measuring the photoresponse. When operating under the conditions of the I-V in Fig.10, we have observed that only the gate on the source side of the device provides a tunable response

when operating in the negative current/voltage quadrant. In the positive current/voltage quadrant, only the drain side gate provides a resonant response. The initial motivation for imaging the active area was to investigate these effects.

Figure 11a shows the beam image, as a filled contour plot, when the split grating-gate detector is biased to I_{SD} = 20μA, V_{SD} = 0.8V, V_G = -0.3V, V_{FG} = -1.04V. This is the same set of conditions as shown for the +20μA photoresponse of Fig. 10, with V_G set to sit on a large resonant peak. In this setup, the detector was positioned as pictured in Fig. 6 so that the grating lines run along the X-direction, while the electric field of the laser is polarized in the Y-direction. The shape of the spot was verified independently, by using a THz beam profiler, to be Gaussian. However, as seen in Fig. 11a, the image is not isotropic. Along the X-direction, the beam seems to map out the 2mm width of the detector, while along the Y-direction, it is clear that something less than the 2mm length of the detector channel is responding to the radiation.

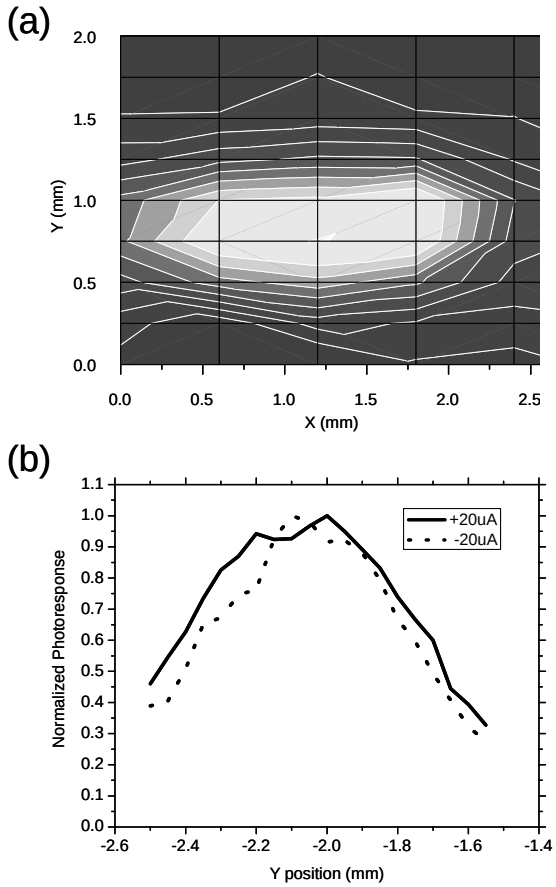

Fig. 11: Results of 1THz beam imaging. (a) V_{FG} = -1.04V, I_{SD}=+20uA, V_G=-0.3V. detector scanned in X and Y. Grating lines run along the X direction. In the X direction, the 2mm size of the detector is clearly mapped out. In the Y direction, it is apparent that less than 2mm of the detector is active leading to the non-isotropic image. (b) Higher resolution scans (on resonance) in the Y-direction only using both positive current and negative current operating points.

To investigate the active region further, higher resolution position scans in the Y-direction were performed while the detector was biased (see Fig. 10) onto the positive current/voltage resonant peak at V_G= -0.3V, and the negative current/voltage resonant peak at V_G=-0.21V respectively. The results are shown in Fig. 11b. While we expected to see a significant shift in the active area between the drain side (positive quadrant, solid trace) and source side (negative quadrant, dashed trace), it appears that the scans are nominally unchanged. One plausible explanation is that only a very small region, near the single finger gate line that bisects the device, contributes to the observed photoresponse.

To investigate the active area more thoroughly, split grating-gate detectors were fabricated with identical grating parameters, 4μm period, 50% duty cycle, 1mm channel width, but with varying channel lengths of 1mm (250 grating lines), 400μm (100 grating lines, and 80μm (20 grating lines). All detectors were made on the same piece of high-quality QW

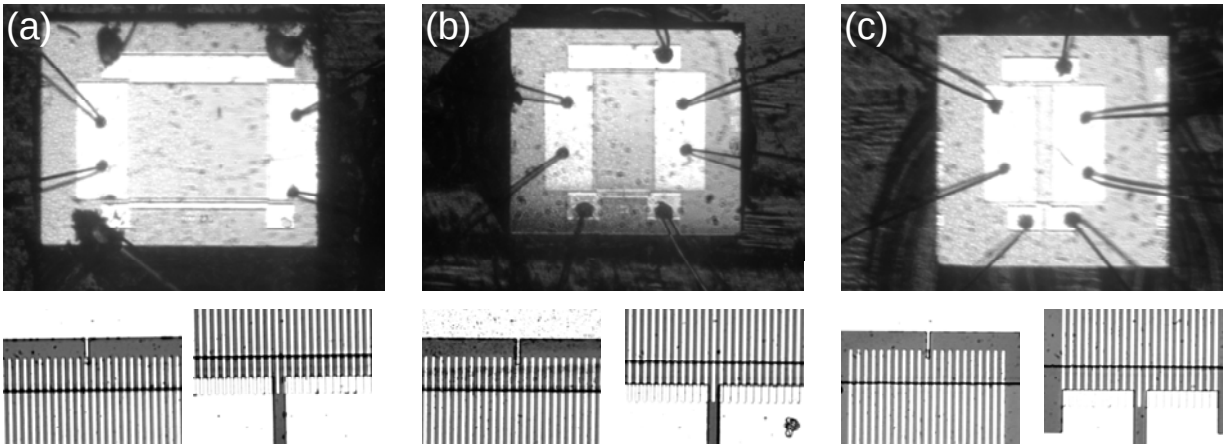

Fig. 12: Detectors used to determine the channel length dependence on the photoresponse. (a) 1mm x 1mm grating, 125 lines on each side of the finger gate. (b) 400μm x 1mm grating, 50 lines on each side of the finger gate. (c) 80μm x 1mm grating, 10 lines on each side of the finger gate. All images were taken using the same magnification to provide a sense of scale. Below each main image are zoomed images of the finger gate (left) and tuning gates (right). Note that in the case of the 80μm long detector (c) the entire grating fits in the zoomed field of view.

material in the same processing run so as to minimize variations that could arise in material or through fabrication. The detectors are pictured in Fig. 12 along with zoomed views of the gate detail below each detector. All bonding pads on the detectors are identical. The source/drain pads are 1mm x 400μm where as the gate connection pads were all of the same vertical dimensions, but varied in length to accommodate the variation in the number of gate lines per device.

Photoresponse measurements were performed, at T=20K, on the three detectors in the manner already described. The main difference in this case was that the illumination frequency was 694GHz instead of 1THz. The beam spot size in this case is now approximately 2.2mm, larger than all detectors in this experiment. For all measurements, the incident power, measured with a Thomas Keating power meter, was approximately 1mW.

The photoresponse for the three different size detectors is displayed in Fig. 13. While there are some clear differences between the measured spectra vs. the tuning gate bias V_G, the main point is clear; the number of grating lines on either side of the single finger gate does not matter a great deal. Looking in particular at the photoresponse near V_G=0V, it only ranges between 2700μV and 3200μV

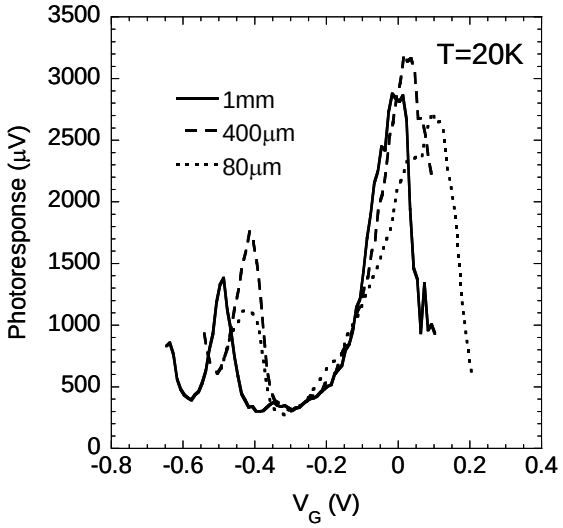

Fig. 13: Response of detectors of varying length, but identical grating parameters. Illumination at 694GHz when operating on a positive current/voltage split-gate operating point.

from detector to detector.

The detector geometries displayed in Fig. 12 have been fabricated from other high mobility single quantum well material. In all cases, we have observed the same trend displayed in Fig. 13. The conclusion drawn here is that, in order to make a more sensitive grating-gate detector, a way must be found to increase the active area of the device so that more of the grating can contribute to the overall photoresponse. While it is plausible that the bonding pads and wires create antennas that couple radiation into the detector, we have not investigated those effects to date. It is possible to fabricate 'center-fed' devices, as will be shown in the next section, which can remove this possibility; however, those devices with varying channel lengths have not been explored at this time. We do note that the results displayed in Fig. 11b for a 2mm x 2mm grating do appear to show that bond pads and wires do not act as antennas, however, as the device dimensions are reduced this may not be the case.

An important detail to note about the shortest channel device (80μm) is that it also had the same noise performance as the longer channel devices. Since both the photoresponse magnitude and the noise are unchanged with length, we can think of noise equivalent power (NEP) in terms of how much radiation is actually hitting the sample. Without considering the area of the sample, the raw NEP of the detectors discussed here is 10^{-7}W/√Hz. However, for the 80 μm detector, less than 1% of the beam is actually hitting the device. When considering only the radiation hitting the sample, this equates to a NEP = 10^{-9}W/√Hz. By itself, that result is not particularly useful as we are trying to make detectors that can be applied in the real world. Hence, being extremely sub-wavelength, as is the 80 μm detector, is not practical since power not absorbed is power lost. Overall though, this result is encouraging as it is very close to our goal NEP for useful detectors and it demonstrates that the potential sensitivity can be achieved if the active area of the detector can be optimized.

2.3 Membrane Style Split Grating-Gate Detector

In the previous section, it was noted that only a small portion of the split grating-gate detector is contributing to the observed photoresponse. In some sense, this is a good thing, because it means there is much room for improvement. On the other hand, the path toward improvement still needs to be revealed. We also noted in the previous section that under certain biasing conditions, the split grating gate detector operates in a bolometric mode. This being the case, we should be able to borrow some tricks from the bolometer field; namely, thermal isolation of the detector element combined with a reduced thermal mass. To reach this end, we made split grating-gate detectors on thermally isolating membranes. In principle, performance enhancement using this technique comes with a cost; one must trade speed for sensitivity. The premise here is that thermal isolation of the detector will allow a larger portion of the grating area to contribute towards heating the center of the device where the bolometric element (the channel underneath the single finger gate) is located.

Devices were fabricated from modulation-doped GaAs/AlGaAs double quantum wells (DQWs). The wells are separated by 70 Å and are each 200 Å wide. The DQW has a combined electron density of 4.14×10^{11} cm^{-2} and low temperature mobility $1 \times 10^6 cm^2/Vs$ determined from Hall

measurements. Two detectors of identical geometry (center fed 1mm x 1mm grating, Fig. 14a) were made from this material. To isolate one of the detectors on a membrane, a backside aligner was used to pattern a square in photoresist on the backside of the chip. Then, a mixture of H_2SO_4:H_2O_2 (1:4) was used to remove approximately 550μm of substrate material. The sample was finished off using Citric Acid(1gm/mL):H_2O_2 (4:1) that etched to an AlGaAs etch stop layer beneath the DQWs. The resulting membrane is approximately 4μm thick. Figure 14b shows the membrane detector with backside IR illumination to emphasize the area that was etched from beneath the detector.

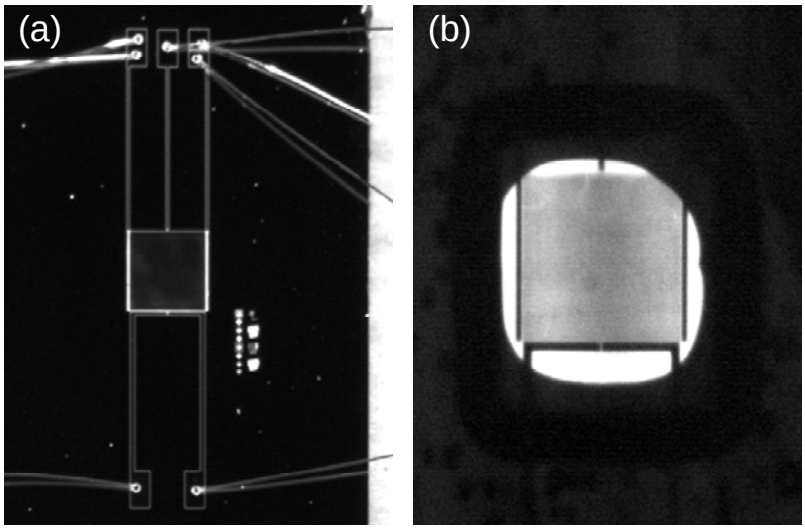

Fig. 14: Split grating-gate detectors made from double quantum well material. (a) The control device made on a thick substrate. Grating lines (not visible) run in the vertical direction. The contact pads for this device are several mm away from the detector which both eliminates antenna effects and allows for membrane isolation of the detector element. (b) The 'membrane' detector with backside illumination used to emphasize the area which has been etched out from behind the detector.

As was the case in Sec. 2.2.1 and 2.2.2, the single finger gate in the split-gate structure was biased beyond pinchoff to create I-V characteristics similar to that of the inset to Fig. 10.

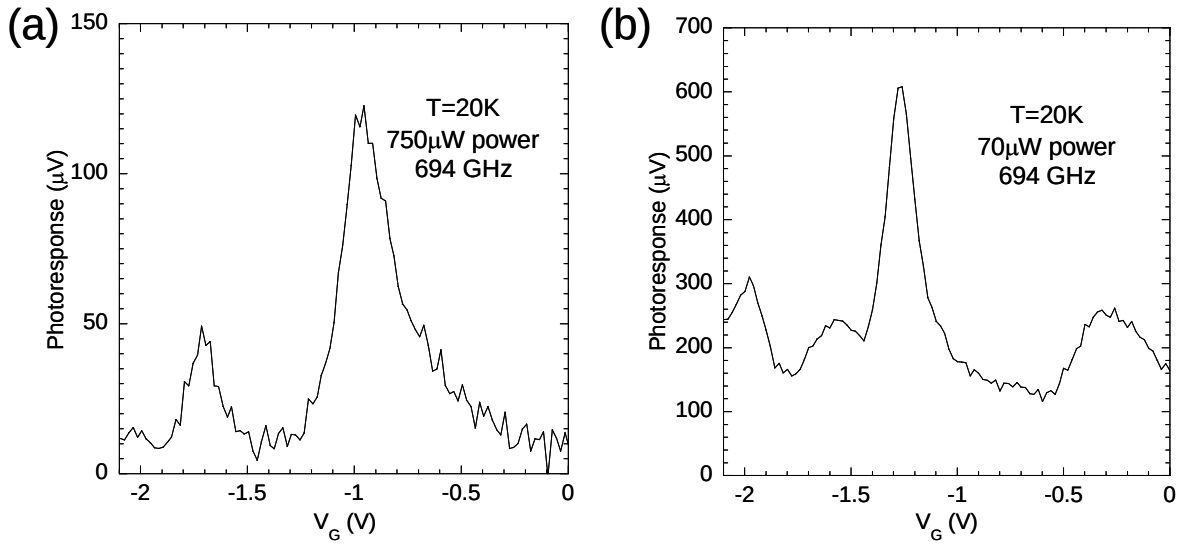

Fig. 15: Photoresponse of 'thick' and 'membrane' detectors. (a) The photoresponse of the 'thick' detector to 750μW of 694GHz radiation. (b) The photoresponse of the 'membrane' detector to only 70μW of 694GHz radiation. The corresponding responsivity increased by a factor of ~45.

Photoresponse measurements were made in the quadrant of positive current/voltage under illumination by a 694GHz laser focused with f/2 optics. Figure 15 shows the rather remarkable difference in responsivity between the two detectors. In Fig. 15a, a maximum resonant response (V_G=-0.95V) of only 120μV to 750μW power (0.16V/W responsivity) is found for the thick detector while in Fig. 15b, approximately 500μV photoresponse (subtracting 100μV background at VG=-1.27V) was found with only 70μW power (7.15V/W responsivity). The membrane detector therefore exhibits ~45X responsivity improvement over its thick counterpart. We have performed this experiment on several matched sets of detectors and obtained the same results every time.

To further understand the improvement in photoresponse introduced by membrane isolation, the thermal transport in the detectors was modeled (details in Appendix C). As shown in Fig. 16a, the thick detector was modeled as a 1 mm diameter, 600 μm tall cylinder with the detector on the top surface and the bottom held at *T*=20 K. The membrane detector, Fig. 16b, was modeled as a 4μm thick disk with its boundary held at T=20K. When considering uniform absorption of power on the detector surface, the center of the thin disk was calculated to have a differential temperature approximately 40 times higher than that of the center of the top of the cylinder. Considering the simplicity of the geometries used, this prediction agrees reasonably well with the factor of 45 improvement observed in photoresponse.

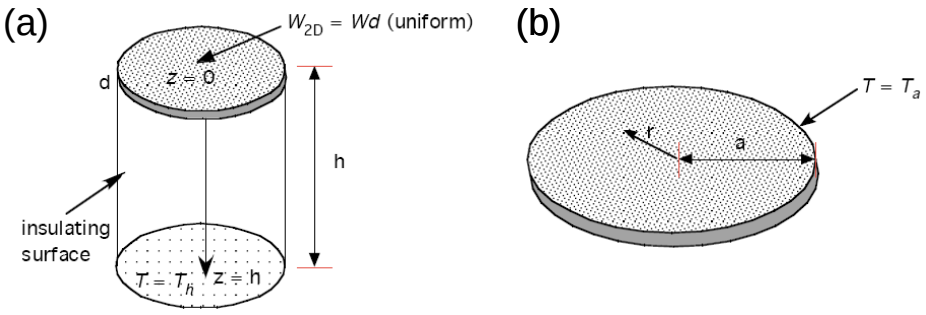

Fig. 16: Model used to simulate thick and membrane detector thermal transport. (a) Thick detector: Insulating cylinder with h=600μm, 1mm diameter, bottom of cylinder held at base temperature. (b) Membrane detector: Disk with diameter of 1mm, thickness 4μm, boundary held at base temperature.

As opposed to the previous section, we now have a case where the responsivity of the detector was increased, while the noise remained the same. Split grating-gate double quantum well detectors have not shown themselves to be as sensitive as their single quantum well counterparts. The NEP of the thick detector was 10^{-6}W/√Hz and the improved NEP of the membrane detector was in the few 10^{-8}W/√Hz range. That being said, there are still obvious ways to gain sensitivity from this point. One being to use single well material, a task currently under way. The reason this was not done from the onset was simply because the membrane process is somewhat low yield and we had more DQW material to use on this project. Beyond that, the membrane used in this work was extremely simple. More complex 'spider web' geometries can be implemented that will provide better thermal isolation.

As mentioned in the beginning of this section, the thermal isolation of the detector can improve sensitivity only by trading off response speed. Our thick detectors, from pulsed measurement

using the free electron laser described in section 2.1, are known to be fast (no slower than 2μs). To test if we had significantly slowed the membrane detector, our radiating chopper speed was varied from 43Hz to 1kHz (it is difficult to modulate THz beams faster than 1kHz as components such as acousto optic modulators do not exist in the THz). Over that frequency range, there was no observed roll-off in the photoresponse, as would be expected if we were nearing the thermal time constant of the system. Pulsed tests on membrane detectors have not been performed to date, although these would be the best way to determine the true time constant of the membrane detector.

3. CONCLUSIONS

While the split grating-gate detector has shown great improvement relative to its single-gate predecessors, the noise-equivalent power (NEP) is currently around 10^{-7}W/√Hz. By illuminating large split grating-gate detectors with THz radiation having a focused spot size smaller than the detector, we have found that the entire detector is not contributing to the photoresponse. By fabricating detectors with varying channel lengths, we have in fact found that the grating area can be shrunk by over 90%, and we still observe the same magnitude of resonant photoresponse. In an attempt to increase the active area of the detector, we have fabricated split grating-gate detectors on thermally isolating membranes from double quantum well material. This led to an improvement by a factor of 45 in the resonant photoresponse and a NEP of 10^{-8}W/√Hz. While there is a great deal of ground left to cover before these detectors can truly compete with Schottky diode detectors (~10^{-10}W/√Hz) in terms of NEP, these findings show that significant improvements may be possible if ways are found to further optimize the active area of the detector.

While we do not yet see a roadblock to further enhancement in sensitivity, there is another path towards detector improvement that has not been explored to date, more efficient optical coupling. We currently believe that only a few percent of incident radiation is absorbed by plasmons in the grating-gate detector channel. The rest simply passes through the material. If this absorption can be increased, the sensitivity would improve concurrently. Surface plasmon based structures, similar to extraordinary transmission gratings, could provide such an effect by binding incident radiation to the interface between the gate metal and the substrate for an increased amount of time and allowing stronger interaction with the underlying detector plasmons. In future work, we plan on investigating this and other concepts to bridge the remaining NEP gap and enable grating-gate detectors to be implemented in spectroscopic THz focal plane arrays.

4. REFERENCES

[1] J.H. Davies, *the Physics of Low Dimensional Semiconductors, An Introduction*. (Cambridge University Press, Cambridge, UK, 1998).

[2] Tsuneya Ando, Alan B. Fowler, and Frank Stern "Electronic properties of two-dimensional systems". *Reviews of Modern Physics* **54**, 437 (1982).

[3] S. J. Allen, D. C. Tsui, and R. A. Logan "OBSERVATION OF 2-DIMENSIONAL PLASMON IN SILICON INVERSION LAYERS". *Phys. Rev. Lett.* **38**, 980-983 (1977).

[4] X. G. Peralta, S. J. Allen, M. C. Wanke, N. E. Harff, J. A. Simmons, M. P. Lilly, J. L. Reno, P. J. Burke, and J. P. Eisenstein "Terahertz photoconductivity and plasmon modes in double-quantum-well field-effect transistors". *Appl. Phys. Lett.* **81**, 1627-1629 (2002).

APPENDIX A: METRICS

- Publications
  - Single-quantum-well grating-gated terahertz plasmon detectors Appl Phys Lett, 87 193507 (2005)
  - Far-infrared spectrum analysis using plasmon modes in a quantum-well transistor IEEE Phot Tech Lett 18: 1925-1927 SEP-OCT (2006)
  - Enhanced responsivity in membrane isolated split-grating-gate plasmonic terahertz detectors Appl Phys Lett, 90 181127 (2007)
- Proceedings
  - Grating gated FET's as narrowband, tunable terahertz detectors P Soc Photo-Opt Ins 5790: 116-122 (2005)
  - Tunable THz detector based on a grating gated field-effect transistor - art. no. 612006
    P Soc Photo-Opt Ins 612006, (2006)
  - Electronically tunable plasmonic grating-gate terahertz detectors P Soc Photo-Opt Ins, 6760-10, (2007) To Be Published

- Invited Presentations
  - APS March Meeting, 2006
  - Princeton University Colloquium, Dec 2006
  - AVS Symposium, May, 2007
  - UMass Lowell, Sept, 2007
- Patents
  - "Terahertz Radiation Mixer" – SD7863/S106113
  - "Electrically Tunable Terahertz Detector" TA# SD7957, Patent application 11/290,090
- Active Collaborations:
  - Jim Allen (UCSB)
  - Greg Aizin (CUNY, theory)

APPENDIX B: PROCESSING INFORMATION

Typical processing matrix for grating gate detectors:

A) Mesa Etch

1) Clean sample by spraying Acetone, IPA and blowing dry
2) Spin AZ5214 resist at 4000RPM/30seconds
3) Bake 90C/90second
4) Remove edge bead by exposing edges for 60seconds. Develop in AZ400K 1:4
5) Expose mesa pattern approximately 5.6 seconds in MJB3 aligner
    a. Mesa pattern must be aligned so that dovetail profile produced by etchant will be on the contact sides
6) Develop using AZ312 1:1.4 for approximately 35seconds
7) Descum in the LFE 5W O2 plasma for 5 minutes
8) Etch in H2SO4:H2O2:H2O 1:8:80 for approximately 50 seconds.
    a. Etch rate is approximately 100A/second. This etch is anisotropic and creats a smooth ramp along one crystal axis and a dovetail groove along the other. The dovetail side should be the corrugated side of the mesa where the contacts will be put down.
9) Clean in Acetone/IPA. Use Aceton spray gun if residual resist is present.

B) Ohmic contact

1) Repeat steps 1-7 of (A) using the 'ohmic' pattern
2) After descum and within 10 minutes before entering evaporation chamber, spray sample for 20 seconds with NH4OH:H2O2 1:20 solution and blow dry (no rinsing)
    a. This removes native oxide and oxide grown in descum
    b. Makes better contacts and also imrpoves metal sticking
3) Evaporate NiGeAuNiAu 80/270/540/140/1500 and liftoff in Acetone
    a. Use Acetone spray gun as needed

C) Gate Step (critical features)

1) Repeat steps 1-6 of (A) using 'Gate' pattern
    a. Don't do the descum, it is not known how that impacts device performance
2) Evaporate Ti/Au 200/500 and liftoff
    a. Soak in Acetone for about ½ hour or more to loosen everything up
    b. Finish with Acetone spray gun

D) Bonding Pads

1) Repeat steps 1-6 of (A) using the 'Pads' pattern
2) Evaporate Ti/Au 200/2000
3) Liftoff in Acetone

Special process for membrane devices:

1) Use crystal bond wax to mount sample face down to a glass slide
2) Spin 5214 resist on the back of the sample
3) Expose and develop a square over the detector using the backside aligner
4) Apply crystal bond wax around the sample edges and on the backside of the sample outside the perimeter of the exposed square

5) Use H2SO4:H2O2 1:4 to etch approximately 550 microns of the substrate
    a. This etchant is CONCENTRATED!
    b. Etch rate about 4 microns per minute. Initial etch rate about 10 microns/minute for the first 100 microns
    c. Use a profiler to measure etch depth, or start a dummy piece 20 minutes prior and wait for that to disappear
6) Rinse sample
7) Mix Citric Acid (1gm/ml):H2O2 ratio 4:1
8) Etch sample until the etch stop layer is reached
9) For unmounting, place the sample at an angle in a beaker of acetone. Eventually, it will slide off
    a. This technique has not caused any membrane fractures. There may be better ways to remove the crystal bond wax, but this works.
10) Place the sample in a beaker of IPA to rinse, then spray it off gently.

APPENDIX C: THERMAL CALCULATIONS FOR MEMBRANE DETECTOR

Heat Transport in Mesoscopic Structures
(from "Heat Conduction," S. K. Lyo, Jan., 2007)

Basic Equation:

$$W(\mathbf{r}) = \frac{d}{dt}(\rho c_v T) - K\nabla^2 T \tag{1}$$

$W(\mathbf{r}) =$ heat generation rate / volume (=uniform)
$\rho =$ mass density, $c_v =$ specific heat, $T =$ temperature,
$K =$ thermal conductivity
In a steady state, Eq. (1) yields

$$W(\mathbf{r}) = -K\nabla^2 T. \tag{2}$$

Quasi-One-Dimensional Cylinder

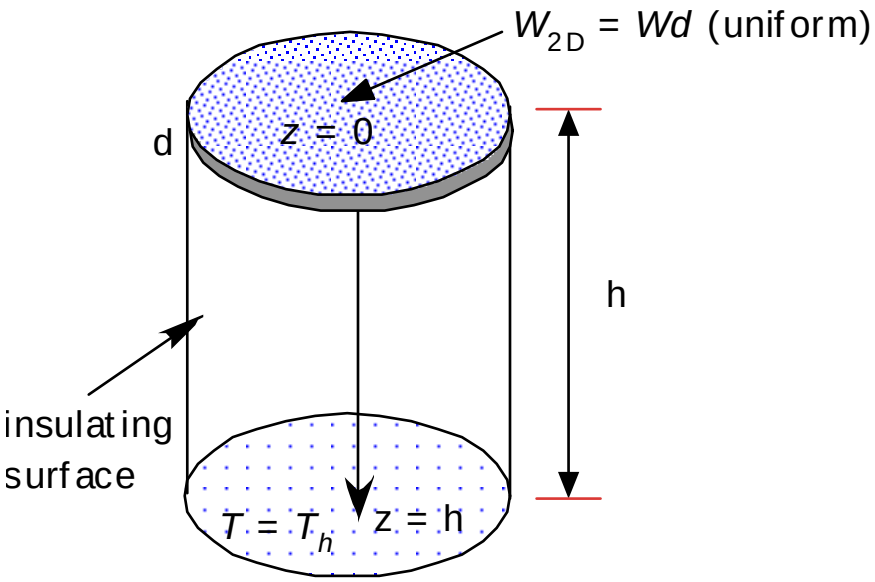

1D cylinder with an arbitrary shaped cross section and a smooth boundary

Fig. 1

The solution is given by

$$z \le d: \; T(z) = -\frac{W}{2K}(z^2 + d^2) + \frac{Wdh}{K} + T_h, \; < T >_{av} = \frac{Wdh}{K}(1 - \frac{2d}{3h}) + T_h$$

$$z \ge d: \; T(z) = -\frac{Wd}{K}(z - h) + T_h, \tag{3}$$

where $<..>_{av}$ denotes the average temperature of the top plate. The temperature at $z = 0$ is given by

$$T(0) = \frac{Wdh}{K}(1 - \frac{d}{2h}) + T_h. \tag{4}$$

In the limit $d << h$, we find naturally $T(0) = <T>_{av}$.

Thin Circular Plate

The circumference of the plate is maintained at $T = T_a$.

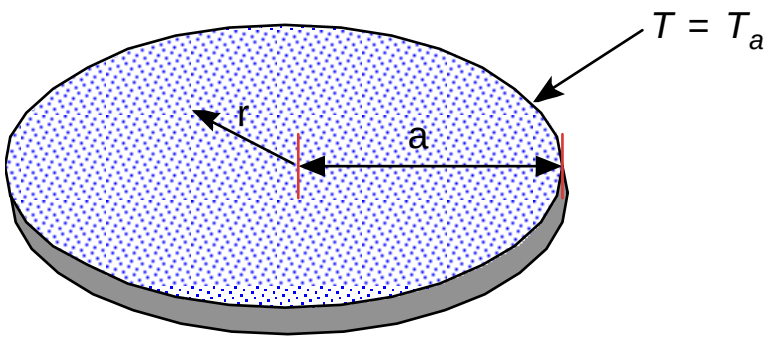

Fig. 2

The solution to

$$W = -K(\frac{d^2T}{dr^2} + \frac{1}{r}\frac{dT}{dr}) \tag{5}$$

is given by

$$T(r) = \frac{W}{4K}(a^2 - r^2) + T_a. \tag{6}$$

The temperature is hottest at the center as expected. Assuming $d << h$, we find

$$\text{Plate}: \quad T(0) = \frac{Wa^2}{4K} + T_a$$

$$\text{Cylinder}: \quad T(0) = \frac{Wdh}{K} + T_h. \tag{7}$$

For $T_a = T_h$ and $a \sim h >> d$, we find that the temperature at the center of the plate is much hotter than at the top of the cylinder.

Thin Rectangular Plate

The following insulating plate absorbs heat uniformly at a rate W per volume. Two vertical sides for the plate are maintained at $T = T_a$, while the other two sides are insulating.

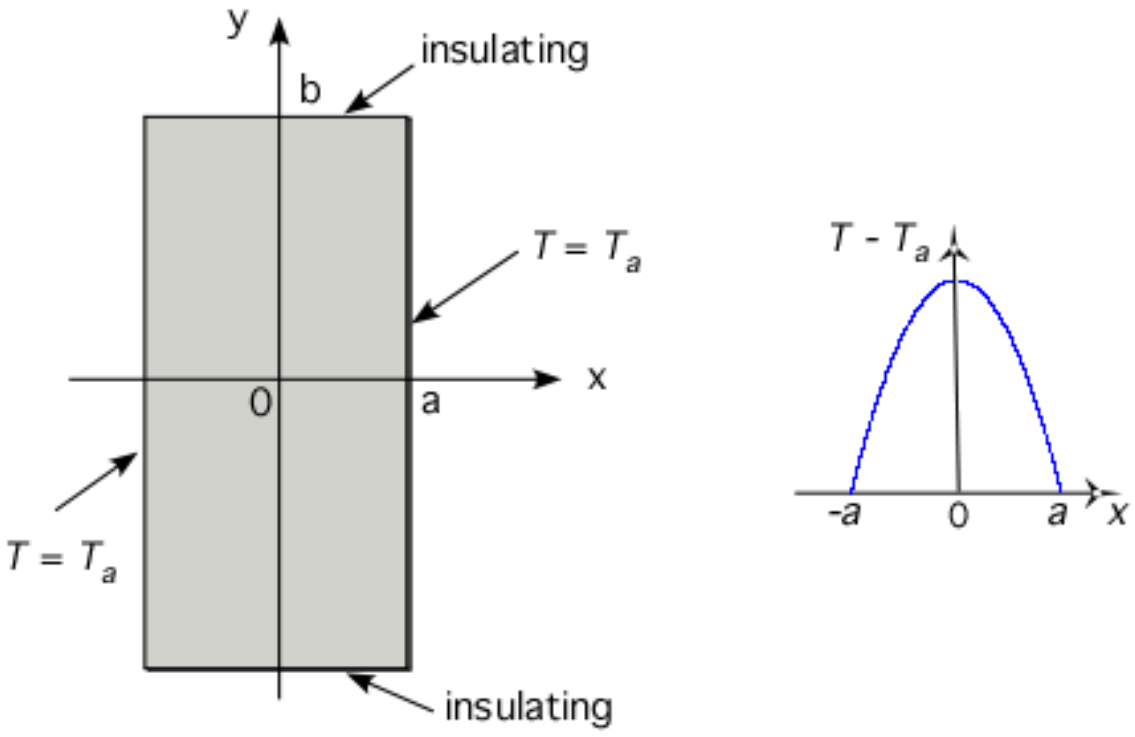

Fig. 3

The solution to Eq. (2) is given by

$$T(x) = \frac{W}{2K}(a^2 - x^2) + T_a. \tag{8}$$

In this case, the temperature is hottest along the vertical center axis $x = 0$. The temperature is independent of the y coordinate. For $T_h = T_a$ in Figs, 1 and 3, we find that the temperature difference

$$T(0) - T_a = \frac{Wa^2}{2K} \tag{9}$$

in the rectangular plate is much larger than that of the cylinder $T(0) - T_h = Wdh/K$ for $a \sim h >> d$.

DISTRIBUTION

1	MS0123	D. Chavez, LDRD Office	1011
1	MS1082	M.C. Wanke	1725
1	MS1082	J.J. Hudgens	1725
1	MS1082	A.D. Grine	1725
1	MS1086	Dan Barton	1123
1	MS1086	Department File	1123
1	MS1303	J.L. Reno	1132
1	MS1415	E.A. Shaner	1123
1	MS1415	S.K. Lyo	1123
1	MS1421	J.A. Simmons	1120
1	MS1427	J.M. Phillips	1100
2	MS9018	Central Technical Files	8944
2	MS0899	Technical Library	9536


Sandia National Laboratories